

Doping effect and oxygen vacancy engineering in nickel-manganese layered double hydroxides for high-performance supercapacitors

Tianpeng Li^a, Yuting Hu^a, Jingyuan Zhang^a, Huajian Li^b, Kun Fang^a, Jiawei Wang^a, Zhuo Wang^a, Ming Xu^{b,*}, Bin Zhao^{a,*}

^a School of Materials & Chemistry, University of Shanghai for Science and Technology, Shanghai 200093, China

^b School of Materials Science and Engineering, State Key Laboratory of Material Processing and Die and Mould Technology, Huazhong University of Science and Technology, Wuhan 430074, China



ARTICLE INFO

Keywords:

NiMn-LDH
Mg Doping
Plasma etching
Oxygen vacancy
Supercapacitor

ABSTRACT

Design of electrode materials with high electrochemical capacitance and long lifetime remains a challenging issue for high-performance supercapacitors. Herein, we successfully synthesized a binder-free composite electrode comprising oxygen vacancy-abundant NiMnMg-layered double hydroxides grown on 3D graphene foam (Vo-NiMnMg-LDH@3DG) by Mg doping during hydrothermal process and subsequently Ar plasma etching. Thanks to the incorporation of electrochemically inert Mg element, the enhanced charge transfer capability, and enriched active sites that induced by plentiful oxygen vacancies, Vo-NiMnMg-LDH@3DG manifests a high specific capacity of 374.8 mAh g⁻¹ at a current density of 1 A g⁻¹ and satisfactory rate performance (74.26% at 20 A g⁻¹). Furthermore, the asymmetric supercapacitor (ASC) assembled with Vo-NiMnMg-LDH@3DG cathode and activated carbon anode exhibits a specific capacitance up to 171 F g⁻¹ at 1 A g⁻¹, achieving a maximum energy density of 53.62 Wh kg⁻¹ and the highest power density of 7500 W kg⁻¹. This work not only provides innovative approaches for preparing oxygen vacancy-rich LDH materials, but also offers insights for the design and improvement of energy storage devices based on transition metal-based LDH.

1. Introduction

With the escalating depletion of conventional energy sources, clean and renewable energy sources, as well as sustainable energy storage devices, are garnering increasing attention. [1–3] As a sustainable and environmentally friendly energy storage solution, electrochemical energy storage (i.e., batteries, capacitors, and supercapacitors) exhibits immense potential and has been extensively researched. [4–6] In comparison to the widely used chemical batteries, supercapacitors, as a novel type of energy storage device, possess the advantages of high reliability, rapid charge and discharge rates, and long-life cycle. However, the low energy density of supercapacitors has hindered their development and practical application to a large extent. [7] The electrode material is a crucial factor influencing the performance of supercapacitors. Currently, a broad range of electrode materials are extensively explored, which include carbon-based materials, transition metal oxides, sulfides, hydroxides, and conductive polymers. [8]

Two-dimensional (2D) materials, such as MXene, graphene and

layered double hydroxides (LDHs), are considered to be promising electrode materials on account of their large specific surface area and excellent structural stability. In particular, owing to the high theoretical capacitance, tunable structure and environmentally friendly nature, LDHs have aroused great interest in recent years. [9,10] However, the poor conductivity and irreversible restacking of these materials often result in unsatisfactory cycling stability and sluggish reaction kinetics, restricting their wide-spread applications. To address these challenges, various strategies have been developed to enhance electrochemical performance of LDHs, including dimensional control, [11] heteroatom doping, [12,13] and compounding with conductive materials. [14,15] Therein, in-situ growth of LDH nano-architecture on conductive supports stands out as a well-established method for improving the electron conductivity of the electrode material. Among various conductive materials, 3D graphene with 3D macroscopic structure consisting of high-crystallinity graphene is regarded as a promising substrate for developing advanced nanocomposite electrodes. [16] In addition, doping non-electroactive metals into LDHs has been reported to be an

* Corresponding authors.

E-mail addresses: ming.xu@hust.edu.cn (M. Xu), zhaobin@usst.edu.cn (B. Zhao).

effective strategy to improve electrochemical performance of supercapacitors. To date, metal elements like Mo, Zn and Al have been successfully incorporated into LDHs as dopants, showcasing potential in augmenting the specific capacitance or cyclic stability of the supercapacitor electrodes. [17–19] Noteworthily, Zhou et al. synthesized ultrathin NiCo-LDH nanosheets doped with Mg, revealing that Mg^{2+} doping promoted charge transfer and adsorption of OH^- in the electrolyte, thereby leading to improved specific capacitance and cyclic life. [20] However, despite this advancement, the cycling stability of the CoNiMg-LDH still fell short of the requirements for commercial applications.

Besides, given that coordinatively unsaturated defects may function as electrochemical active sites, delicate control of the defect structure can be highly effective in enhancing the electrochemical energy storage performance of LDHs. [21–23] Especially, oxygen vacancies have been reported to play a crucial role in electrode materials by improving the electrical conductivity, and promoting exposure of more active surface area, thereby contributing to superior rate capacity and high specific capacitance. [24–27] For example, Li et al. revealed that irreversible redox of Co cations in NiCo carbonate hydroxide induced the formation of oxygen-vacancy-rich NiCo-LDH, which demonstrated excellent high-rate energy storage capability. [27] Furthermore, oxygen vacancies can also increase the interaction between LDHs and OH^- ions in the electrolyte, which is beneficial for the insertion/extraction of OH^- in the host layer of LDHs. [18,28,29] Nevertheless, in spite of the extensive efforts devoted, a fabrication strategy for finely controlling oxygen vacancy in LDHs without destroying the structure is still lacking. Recently, plasma etching has emerged as an ideal technique for inducing oxygen vacancy in LDHs due to its unique advantages, such as being time-saving and free from chemical contaminants. [30] But to the best of our knowledge, plasma-induced defect engineering in LDHs for high-performance supercapacitor is still rarely reported.

Herein, by combining the aforementioned strategies, oxygen vacancy-rich and free-standing NiMn-LDH nanocomposite electrodes were synthesized through a two-step process. Firstly, Mg-doped NiMn-LDH nanosheets were in situ grown on 3D graphene using a facile hydrothermal method. Subsequently, abundant oxygen vacancies were introduced to the LDHs via Ar plasma etching, resulting in the formation of defect-rich composites (designated as Vo-NiMnMg-LDH@3DG). Leveraging the synergistic effects of conductive graphene and Mg-doped NiMn-LDH, the Vo-NiMnMg-LDH@3DG demonstrates a high specific capacity up to 374.8 mAh g^{-1} at 1 A g^{-1} and remarkable rate performance (278.3 mAh g^{-1} at 20 A g^{-1}). Besides, the composite electrode also shows excellent cycling stability with 92.6% capacity retention after 12,000 cycles. Furthermore, the asymmetric supercapacitors (ASCs), constructed with Vo-NiMnMg-LDH@3DG as the positive electrode and commercially available activated carbon (AC) as the negative electrode, delivers a high specific capacitance of 171 F g^{-1} at a current density of 1 A g^{-1} , along with a maximum energy density of 53.62 Wh kg^{-1} and the highest power density of 75.00 W kg^{-1} . This work not only provides a new approach for preparation of oxygen vacancy-rich LDH materials, but also sheds light on the rational design and improvement of transition metal-based LDH electrodes.

2. Results and discussion

Fig. 1 schematically illustrates the synthesis process of the composites. Firstly, three-dimensional graphene (3DG) was grown by chemical vapor deposition using nickel foam as both the catalyst and substrate. Then, Mg-doped NiMn-LDH was in situ synthesized on 3DG by a simple hydrothermal method, with the Mg dopant substituting some of the metal cations in the host layer of LDH. Subsequently, Ar plasma etching was employed to introduce more oxygen vacancies into LDH. To obtain better electrochemical performance, Mg doping concentration in the NiMn-LDH was firstly optimized. As shown in **Figure S1a** and b, the NiMnMg-LDH@3DG synthesized with a Mg precursor of 0.11 mmol ($NiMnMg_{0.11}$ -LDH) exhibits the highest specific capacity. Moreover, $NiMnMg_{0.11}$ -LDH also demonstrates the superior rate capability and faster ion diffusion kinetics (**Figure S1c, d**, **Table S1**). Consequently, $NiMnMg_{0.11}$ -LDH was used for subsequent experiments. Hereafter, unless otherwise specified, NiMnMg-LDH refers to the $NiMnMg_{0.11}$ -LDH.

Field-emission scanning electron microscopy (FE-SEM) was employed to observe morphology of the as-obtained samples. As depicted in **Fig. 2a** and b, Mg doping did not change the honeycomb nanosheet morphology of LDH, and both the NiMn-LDH and NiMnMg-LDH exhibit a vertically grown and cross-linked honeycomb nanosheet morphology on Ni foam. The samples prepared with different Mg doping concentrations also display similar morphologies (**Figure S2**). However, compared to NiMn-LDH@3DG (**Fig. 2a**), the nanosheets in NiMnMg-LDH@3DG appear denser and smaller in lateral size (**Fig. 2b**), indicating a larger specific surface area. After plasma treatment, the nanosheets are well preserved and no fragmentation and collapse are observed in Vo-NiMnMg-LDH@3DG, meanwhile the thickness of the nanosheets is obviously reduced (**Fig. 2c**). Microstructure of the pristine and plasma-treated NiMnMg-LDH@3DG was further examined by transmission electron microscopy (TEM). Typically, ultrathin nanosheets with distinct wrinkles are observed for both samples (**Fig. 2d, e**, **Figure S3a, b**), indicating that plasma treatment did not disrupt the LDH structure. In the high-resolution TEM (HR-TEM) images shown in **Fig. 2f** and **Figure S3c**, lattice fringes with an interplanar distance of 0.27 and 0.39 nm can be clearly observed, corresponding to the (015) and (006) plane in NiMnMg-LDH, respectively. Unusually, some curved lattice fringes are noticeable, as shown in the inset of **Fig. 2f**, directly indicating structural disorder in the LDH. [31] **Figure S4** presents the selected-area electron diffraction (SAED) pattern of the Vo-NiMnMg-LDH@3DG. The appearance of diffraction rings suggests the polycrystalline nature of NiMnMg-LDH. The pristine sample displays a similar SAED pattern (**Figure S4d**). Energy dispersive X-ray spectroscopy (EDS) spectra (**Figure S5**) provide evidence of the atomic composition in the pristine NiMn-LDH/3DG and the successful doping of Mg in NiMnMg-LDH/3DG, with an Ni/Mg atomic ratio of 7.3:1. Furthermore, plasma treatment does not alter the atomic composition of the LDHs. The elemental mapping reveals uniform distribution of Ni, C, Mn, Mg, O elements in the Vo-NiMnMg-LDH@3DG, indicating the successful synthesis of NiMnMg-LDH on 3DG (**Fig. 2g**). Presence of the Cl element can be attributed to the interlayer Cl^- in the LDH materials.

The crystal phases of the as-prepared samples were characterized by

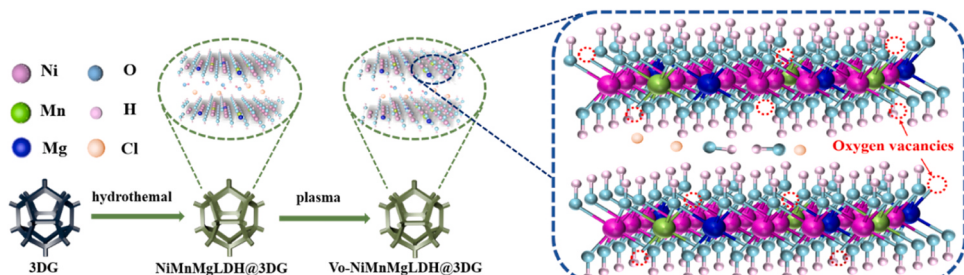


Fig. 1. Schematic diagram illustrating synthesis process of Vo-NiMnMg-LDH@3DG composites.

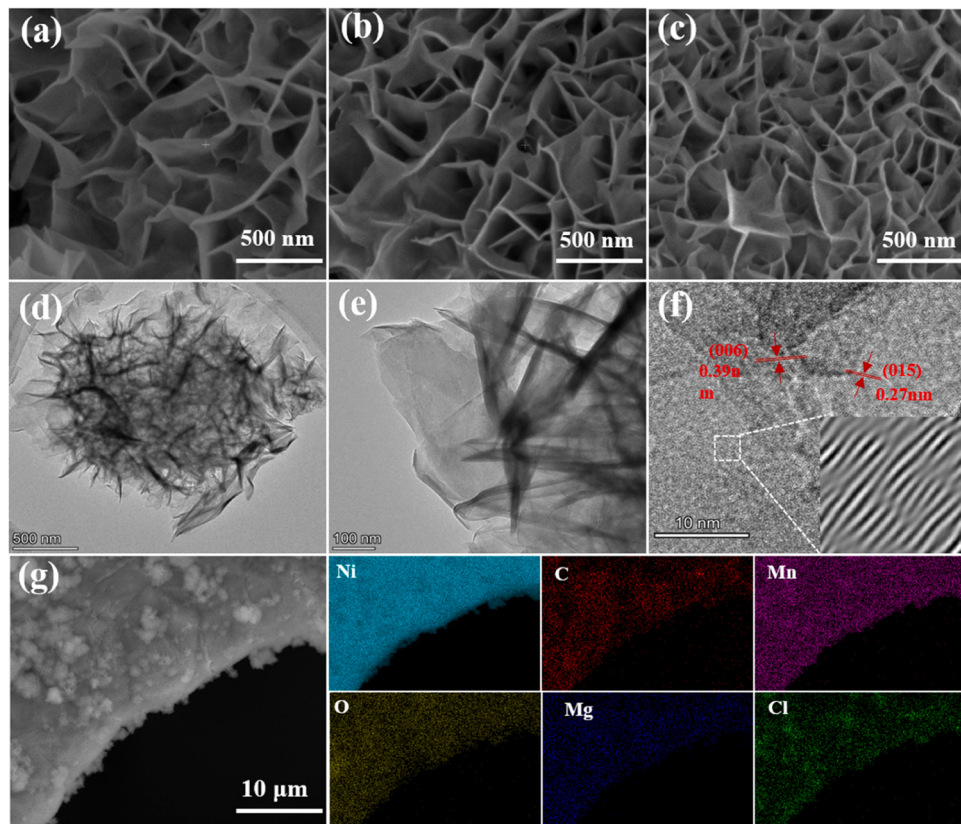


Fig. 2. FE-SEM images of (a) NiMn-LDH@3DG, (b) NiMnMg-LDH@3DG, and (c) Vo-NiMnMg-LDH@3DG. (d, e) TEM images of Vo-NiMnMg-LDH@3DG with different magnifications. HR-TEM image (f) and EDS elemental mapping (g) of Vo-NiMnMg-LDH@3DG.

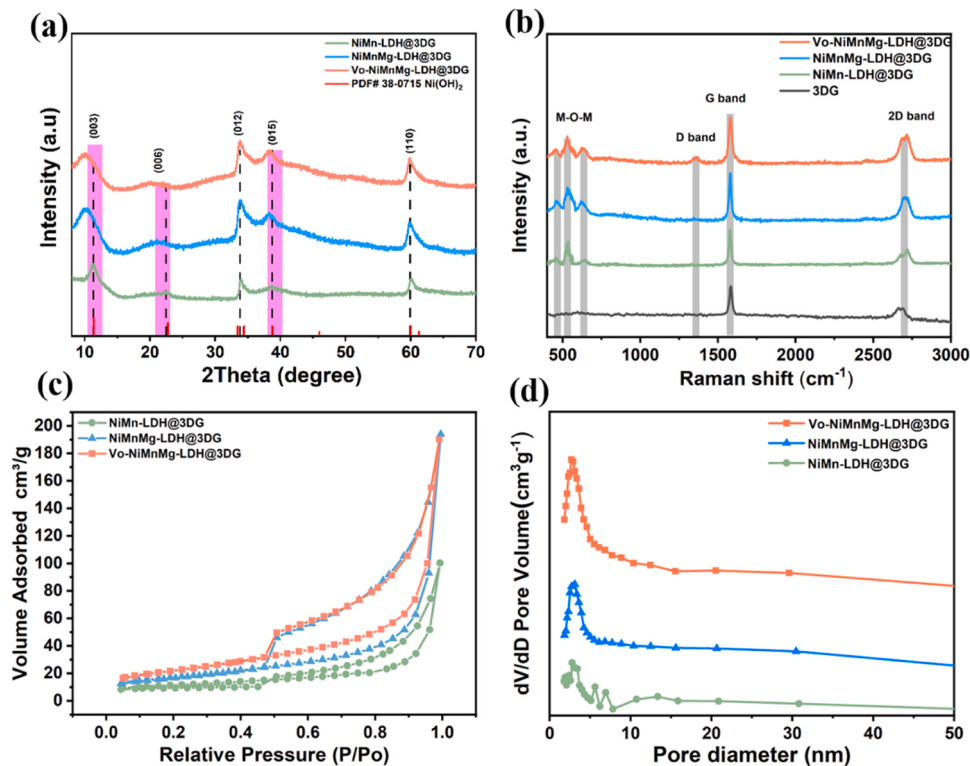


Fig. 3. (a) XRD patterns, (b) Raman spectra, (c) N_2 adsorption-desorption isotherm and (d) pore-size distribution of NiMn-LDH@3DG, NiMnMg-LDH@3DG and Vo-NiMnMg-LDH@3DG.

X-ray diffraction (XRD). Fig. 3a shows XRD patterns of NiMn-LDH@3DG, NiMnMg-LDH@3DG and Vo-NiMnMg-LDH@3DG composites. For the NiMn-LDH@3DG, the diffraction peaks at 11.3° , 22.7° , 33.5° , 38.8° and 60.0° are well assigned to the (003), (006), (012), (015) and (110) crystal planes of the Ni(OH)₂ (JCPDS No.38-0715), [32,33] respectively. After Mg doping, no additional diffraction peaks are discerned, indicating the possible dissolution of Mg atoms into the NiMn-LDH lattice by substituting some Ni/Mn cations in the host layers. The broadening and slight shift towards the lower angles in the (003) and (006) peaks indicate the increased interlayer distances and lower crystallinity resulting from Mg doping. [34] It is worth mentioning that the expanded interlayer space may facilitate fast transport of electrolyte ions. As the feeding ratio of Mg precursor increases, both peaks shift further to lower 2θ values (Figure S6), attributed to greater presence of Mg dopants in the LDH. Besides, a careful examination of Fig. 3a reveals that plasma etching does not alter the crystal phase of LDH, but induces broader diffraction peaks compared to the pristine NiMnMg-LDH@3DG, indicating degraded crystallinity and increased vacancies upon plasma treatment. [35] Raman analysis was further carried out to gain more structural information of the as-prepared nanocomposites. As illustrated in Fig. 3b, the prominent G band at 1590 cm^{-1} and the absence of the D-band around 1360 cm^{-1} demonstrate the high quality of CVD-grown graphene. The 2D-band at 2700 cm^{-1} is associated with the lattice vibrations of the two phonons. [36] The intensity ratio of 2D to G bands (I_{2D}/I_G) of ~ 0.4 signifies presence of the few-layer graphene.[37] In addition, the characteristic peaks at 455 , 530 and 635 cm^{-1} are visible for NiMn-LDH@3DG, NiMnMg-LDH@3DG and Vo-NiMnMg-LDH@3DG, which can be ascribed to A_{1g} vibration of Ni-OH, A_g vibration of Ni-O, and vibrational stretching mode of Mn-O. [38–41] Nitrogen adsorption-desorption isotherms were also employed to characterize the specific surface area and pore size distribution of different composites. As depicted in Fig. 3c, all the LDH samples exhibit a type-IV isotherm with a H3-type hysteresis loop, indicative of mesoporous structure characteristics. The specific

surface area (SSA) values for NiMn-LDH, NiMnMg-LDH and Vo-NiMnMg-LDH are 38.7 , 60.2 and $78.4\text{ m}^2/\text{g}$, respectively. Notably, the SSA of NiMnMg-LDH and Vo-NiMnMg-LDH reach 1.6 and 2.0 times that of NiMn-LDH, respectively, suggesting that Mg doping and plasma etching can increase the specific surface area of the material effectively, which might be credited to the lattice distortion and defects induced by doping and plasma etching. [42] The pore size distribution obtained using the BJH method is shown in Fig. 3d. Clearly, the NiMn-LDH@3DG, NiMnMg-LDH@3DG and Vo-NiMnMg-LDH@3DG show similar mesopore-dominant structure with the average pore size of 16.03 , 19.94 and 14.98 nm , respectively (as listed in Table S2). In short, the above-mentioned results suggest that Mg doping induces degraded crystallinity and structural disorder in the lattice, while simultaneously increasing specific surface area of NiMn-LDH. These effects can be further intensified by plasma etching. Undoubtedly, the combined impact of Mg doping and plasma treatment is conducive to exposing more active sites.

X-ray photoelectron spectroscopy (XPS) was utilized to further explore chemical composition and elemental valence states on the surface of NiMn-LDH@3DG, NiMnMg-LDH@3DG and Vo-NiMnMg-LDH@3DG. Fig. 4a shows survey spectra of the NiMn-LDH@3DG, validating the existence of C, O, Ni and Mn elements. For the other two samples doped with Mg, the presence of Mg element is also detected. In Ni 2p high-resolution spectrum, two spin-orbit peaks of Ni 2p_{3/2} and Ni 2p_{1/2} and two shake-up satellites are clearly observed for NiMn-LDH@3DG, NiMnMg-LDH@3DG and Vo-NiMnMg-LDH@3DG (Fig. 4b). Each spin-orbit peak can be well fitted into two peaks, suggesting the co-existence of Ni²⁺ and Ni³⁺.[43,44] Importantly, compared with the NiMn-LDH, the Ni²⁺/Ni³⁺ ratio increases in NiMnMg-LDH@3DG and Vo-NiMnMg-LDH@3DG. Specifically, the Ni²⁺/Ni³⁺ ratio rises from 2.42 to 3.08 after Mg doping and further increases to 3.59 upon plasma treatment (Table S3). These results indicate that the incorporation of Mg and plasma treatment could reduce the high-valence Ni³⁺ to Ni²⁺ and promote the extraction of lattice

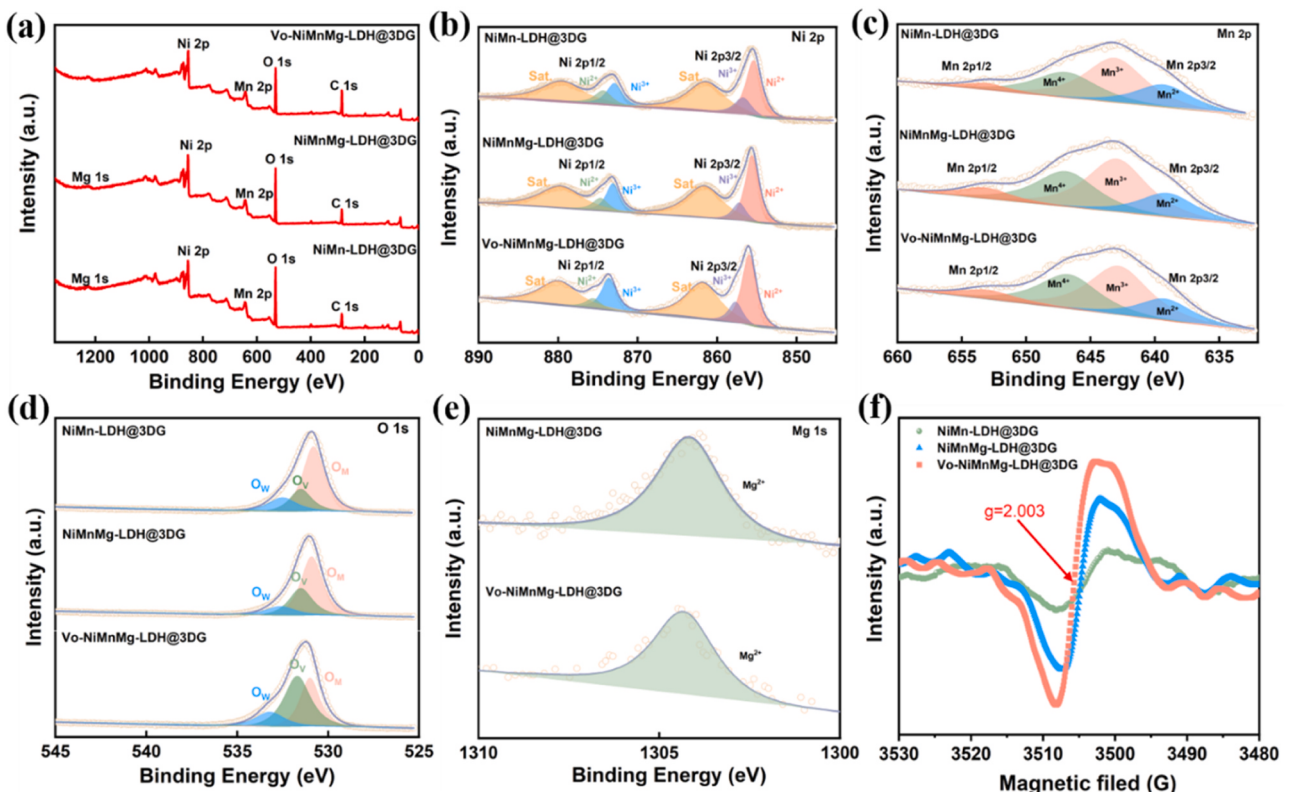


Fig. 4. XPS spectra of NiMn-LDH@3DG, NiMnMg-LDH@3DG and Vo-NiMnMg-LDH@3DG: (a) Survey spectrum, (b) Ni 2p, (c) Mn 2p, (d) O 1 s, (e) Mg 1 s. (f) EPR spectra of NiMn-LDH@3DG, NiMnMg-LDH@3DG and Vo-NiMnMg-LDH@3DG.

oxygen, thus inducing the formation of oxygen vacancies. [45,46] In the Mn 2p high-resolution spectrum (Fig. 4c), the Mn 2p_{3/2} is deconvolved into three peaks with binding energies of 639.1, 643.0, and 646.8 eV corresponding to Mn²⁺, Mn³⁺, and Mn⁴⁺, respectively. It is evident that there is no significant change in the percentage of peak areas of Mn²⁺, Mn³⁺ and Mn⁴⁺ for the three samples. [47,48] As presented in Fig. 4d, the O 1 s spectrum can be deconvoluted into three peaks. Specifically, the peak at 530.8 eV is associated with metal-oxygen bond (O_M), the peak centered at 531.3 eV is attributed to defect sites with a low oxygen coordination (O_v), and the one at 532.4 eV is due to surface absorbed water (O_w). [18,49,50] Table S4 summarizes the change in the percentage of the O species. Obviously, in comparison with NiMn-LDH, the content of O_M decreases, while the proportion of O_v increases noticeably (from 21.8% to 30.4%) in NiMnMg-LDH. This suggests that Mg doping induces a change in the coordination environments around the metal atoms and produces abundant oxygen vacancies. Upon plasma treatment, more oxygen vacancies are generated owing to the bombardment of Ar ions, and the percentage of O_v further rises to 45.8%. Regarding the Mg 1 s high-resolution spectrum (Fig. 4e), the binding energy at 1304.5 eV indicates the existence of Mg²⁺ in the LDH. [51] Electron paramagnetic resonance (EPR) was also used for the characterization of oxygen vacancies in the three samples (Fig. 4f). A stronger signal at g= 2.003 indicates a larger amount of oxygen vacancies in NiMnMg-LDH@3DG than in NiMn-LDH. Following plasma treatment, the concentration of oxygen vacancies further increases, accompanying by a more intensified signal in Vo-NiMnMg-LDH@3DG. [18,52,53] These results are in agreement with the XPS analysis. Taken together, the results demonstrate that Mg doping induces a redistribution of the surface electronic structure of the LDH, leading to the emergence of oxygen vacancies to maintain charge balance. And the subsequent plasma treatment induces the departure of additional lattice oxygen, thereby introducing a higher concentration of oxygen vacancies.

Electrochemical properties of the various LDH composites were evaluated using cyclic voltammetry (CV) and galvanostatic charge-discharge (GCD) in a conventional three-electrode system with 2 M

KOH aqueous electrolyte. Fig. 5a shows CV curves of the NiMn-LDH@3DG, NiMnMg-LDH@3DG and Vo-NiMnMg-LDH@3DG at a scan rate of 5 mV s⁻¹. Compared with NiMn-LDH@3DG, the Mg-doped composite exhibits a larger enclosed area within the CV curve, indicating an enhanced capacitive behavior. After plasma etching, the CV integral area is further increased, revealing superior capacitive performance for Vo-NiMnMg-LDH@3DG. The two oxidation peaks at 0.41 V and 0.47 V correspond to the oxidation processes of Ni and Mn, respectively. [54] Interestingly, compared with NiMn-LDH@3DG, the anodic peak around 0.47 V becomes more pronounced in NiMnMg-LDH@3DG, which further intensifies after plasma treatment. This result suggests the possible activation of Mn sites in the LDHs by the oxygen vacancies. Moreover, for Vo-NiMnMg-LDH@3DG, the current response increases accordingly as the scan rate rises, with a similar shape in the CV curves (Figure S7a), suggesting outstanding rate performance. [49] GCD measurements also demonstrate the similar results. As depicted in Fig. 5b, among the three composite electrodes, Vo-NiMnMg-LDH shows the longest discharge time at a current density of 1 A g⁻¹, suggesting the largest specific capacity. Also, the presence of two distinct voltage plateaus around 0.41 and 0.47 V (vs. Hg/HgO) further verify the faradaic redox characteristics of these LDH composites, coinciding with the CV results. For Vo-NiMnMg-LDH@3DG, the symmetric GCD profiles at various current densities further indicate excellent reversibility and high coulombic efficiency (Figure S7a, b). Fig. 5c shows the specific capacitance of the composite electrodes at various current densities. Apparently, at each current density from 1 to 20 A g⁻¹, the specific capacitance follows the sequence of Vo-NiMnMg-LDH@3DG>NiMnMg-LDH@3DG>NiMn-LDH@3DG, demonstrating the beneficial impact of Mg doping and plasma treatment in enhancing electrochemical performance. Specifically, the specific capacity of Vo-NiMnMg-LDH is 374.8, 352.2, 332.7, 313.1, 302.1, and 278.3 mAh g⁻¹ at the current density of 1, 2, 4, 8, 10 and 20 A g⁻¹, respectively. That is to say, as the current density increases from 1 to 20 A g⁻¹, 74.26% of the initial capacitance is still retained, manifesting the excellent rate capability. It is noteworthy that such a high specific

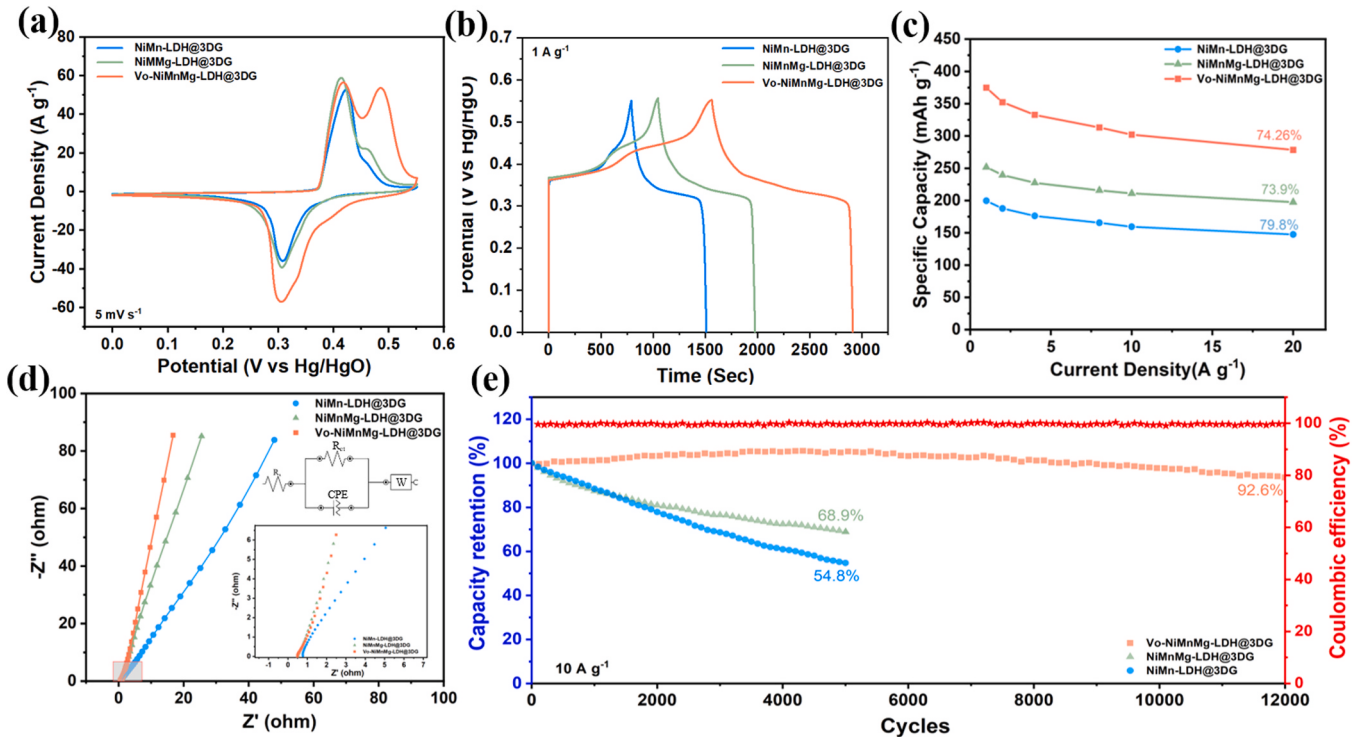


Fig. 5. Electrochemical performance of various composite electrodes in 2 M KOH: (a) CV curves at a scan rate of 5 mV s⁻¹, (b) GCD curves at 1 A g⁻¹, (c) Specific capacity at various current densities, (d) Nyquist plots, (e) Cycling performance at 10 A g⁻¹.

capacity of 374.8 mAh g⁻¹ exceeds the vast majority of LDH-based electrode materials (Table S5), such as Ov-NiMn-LDH (1183 C g⁻¹) [49], NiMn-LDH-O (1082 C g⁻¹), [54] CoNiMg-LDH (1095.2 C g⁻¹), [42] Mn/NiCo-LDH (518 C g⁻¹), [38] NiMn-LDH/PC (1634 F g⁻¹), [55] and NiMn-LDH/MXene (1575 F g⁻¹). [56]

To better understand the impact of oxygen vacancies, electrochemical impedance spectroscopy (EIS) measurements were further conducted. As shown in Fig. 5d, the Nyquist plots of all the samples show negligible semicircles in the high-frequency region, indicating that the charge transfer resistance (R_{ct}) at the electrode/electrolyte interface is quite small with the assistance of the highly conductive graphene network. Besides, by the intersection of the plot with the real axis, the equivalent series resistance (R_s) can be determined. Interestingly, all the composites exhibit small R_s values less than 1 Ω, suggesting good electron transfer capability (Table S6). In comparison to NiMn-LDH@3DG (0.78 Ω), the Mg-doped composite has a smaller R_s value (0.51 Ω), indicating that Mg doping improves the electrical conductivity of the electrode material effectively. After plasma treatment, an even smaller R_s (0.48 Ω) is achieved in Vo-NiMnMg-LDH@3DG, possibly due to the increased concentration of oxygen vacancies. In addition, the steeper slope in the low-frequency area for Vo-NiMnMg-LDH@3DG represents the smaller Warburg impedance (Z_w) and faster ion transport rate than the other samples. [37] Possibly, the increased SSA and more mesoporous structure induced by Mg doping and plasma etching facilitate diffusion of electrolyte ion in the electrode. [57]

Considering the positive effect of plasma treatment on electrochemical performance, the duration of plasma treatment was further optimized. And the sample treated with Ar plasma for different durations (10, 30 and 60 s) is designated as NiMnMg-LDH@3DG-10 s, NiMnMg-LDH@3DG-30 s and NiMnMg-LDH@3DG-60 s, respectively. As presented in Figure S8, all the plasma-treated LDH materials exhibit a larger enclosed area in the CV curve and longer discharge time than the pristine NiMnMg-LDH, signifying the improved capacitive properties. Based on the calculated specific capacity (Figure S8c), NiMnMg-LDH@3DG-30 s manifests the largest specific capacity at all current densities than the counterparts, indicating its superior supercapacitive performance. Moreover, EIS tests also suggest the smallest R_s , R_{ct} and favorable Z_w for NiMnMg-LDH@3DG-30 s (Figure S8d, Table S7). Therefore, 30 s is selected as the optimal plasma treatment duration in this work.

Fig. 5e presents cycling stability of the various composite electrodes. After Mg doping, the stability of NiMnMg-LDH@3DG displays a noticeable improvement over the original NiMn-LDH. And plasma treatment further enhances the cycling stability of the LDH composite. Specifically, after 5000 cycles at the current density of 10 A g⁻¹, the specific capacity of NiMnMg-LDH@3DG retains at 68.9%, whereas NiMn-LDH@3DG only retains 54.8% of its specific capacity. This observation directly demonstrates the advantage of Mg doping in enhancing the cycling stability. Given that non-electroactive Mg does not participate in the redox reaction during charge/discharge, and magnesium hydroxide is highly stable in alkaline medium, [13,42] the incorporation of Mg in the host layer stabilizes the lattice structure of LDH in electrochemical process. Encouragingly, after plasma treatment, Vo-NiMnMg-LDH@3DG exhibits exceptional stability over long-term cycling, retaining 92.6% of its capacitance after 12,000 cycles. These results provide irrefutable evidence of the efficacy of our two-step strategy in enhancing the electrochemical performance of NiMn-LDH@3DG.

The excellent capacitive performance Vo-NiMnMg-LDH@3DG can be attributed to the unique structural characteristics. Firstly, in-situ growth of LDH on high-quality graphene foam ensures the intimate contact between LDH and graphene, facilitating efficient electron conduction and preventing shedding of the active materials. Secondly, doping of non-electroactive Mg stabilizes the crystal lattice of LDH material, thus improving the long-term stability. [20] Thirdly, Mg doping and plasma treatment increase the specific surface area and

exposes more active sites, thus promoting the charge storage capacity. Ultimately, Mg doping and subsequent plasma treatment induce abundant oxygen vacancies in the LDH, which not only enhance the electrical conductivity and boost charge transfer rate, but also reduce the adsorption energy of OH⁻, leading to a significant improvement in the capacitive performance. [49]

To further explore the influence of mass loading on electrochemical performance, composite electrode with larger mass (1.5, 2.3 and 4 mg cm⁻²) was also synthesized. Figure S13 presents CV and GCD curves of the various composite electrodes. The specific capacity at different current densities for these composite electrodes is compared in Figure S14. It is evident that an increase in the mass of active material leads to a decrease of the specific capacity and rate performance. SEM observation reveals that with increasing the mass loading, more spherical structures consisting of agglomerated nanosheets are formed on the electrode surface (Figure S15), which may result in poor mass and electron transport in the electrode. Moreover, since plasma treatment is only effective for exposed surface, an excessively thick LDH layer may counteract the positive effect of plasma etching on the active materials. Despite the obvious decrease in the capacitive performance of the high-mass-loading electrode, the specific capacity of 245 mAh g⁻¹ (1604 F g⁻¹) for the Vo-NiMnMg-LDH@3DG-4 is still competitive compared to many previously-reported results (Table S5).

To gain more insights into the greatly enhanced supercapacitive performance of Vo-NiMnMg-LDH@3DG, electrochemical kinetics was investigated by CV measurements from 1 to 50 mV s⁻¹. According to the power-law relationship between the peak current density (i , A g⁻¹) and the scan rate (v , mV s⁻¹) [58]:

$$i = kv^b \quad (1)$$

the parameter b can be determined. Generally, a b-value of 0.5 represents a diffusion-controlled process and the value of 1 indicates a surface-controlled capacitive process. As depicted in Figure S9, the calculated b-values from the oxidation and reduction peaks are 0.58 and 0.66, respectively, suggesting the diffusion-controlled charge storage behavior. Then, the capacitive contribution at different scan rates can be calculated using the equation [59]:

$$i = k_1 v + k_2 v^{1/2} \quad (2)$$

where $k_1 v$ and $k_2 v^{1/2}$ correspond to surface capacitive effect and diffusion-controlled contribution, respectively. The shaded area in Fig. 6a represents the surface capacitive contribution at the scan rate of 1 mV s⁻¹, which occupies approximately 36.22% of the total capacity. As the scan rate increases, the capacitive contribution increases gradually and finally reaches 55.36% at 20 mV s⁻¹ (Fig. 6b), revealing that the capacitive charge storage becomes dominant at high scan rate. Both NiMnMg-LDH@3DG and NiMn-LDH@3DG exhibit similar electrochemical kinetic behavior (Figure S10, Figure S11).

In order to unveil the energy storage mechanism, in-situ Raman spectroscopy was performed to monitor structural change of Vo-NiMnMg-LDH@3DG during charge-discharge in KOH electrolyte. In the initial state, the three characteristic peaks at 455, 531 and 635 cm⁻¹ correspond to the vibration of Ni-OH, Ni-O and Mn-O, respectively (Figure S12). [40,41] As the charging process proceeds, these peaks remain present until 0.3 V, and the two new peaks at 472 (peak 1) and 553 cm⁻¹ (peak 2) that emerge above 0.3 V are well assigned to NiOOH, suggesting the transformation from Ni(OH)₂ to NiOOH during charging. [38] Then, as the potential rises, both peaks gradually intensify. Notably, when the potential is higher than 0.4 V, the peak of Mn-O stretching vibration shifts from 635 to 616 cm⁻¹, attributed to the conversion of Mn-O species to MnOOH, [60] which is consistent with the anodic peak in the CV curve at 1 mV s⁻¹ (Fig. 6c). During the discharge process, the intensity of the two NiOOH peaks gradually weakens and ultimately vanishes, accompanying the recovery of the original three peaks. Fig. 6c and d illustrate the intensity variation of the two NiOOH

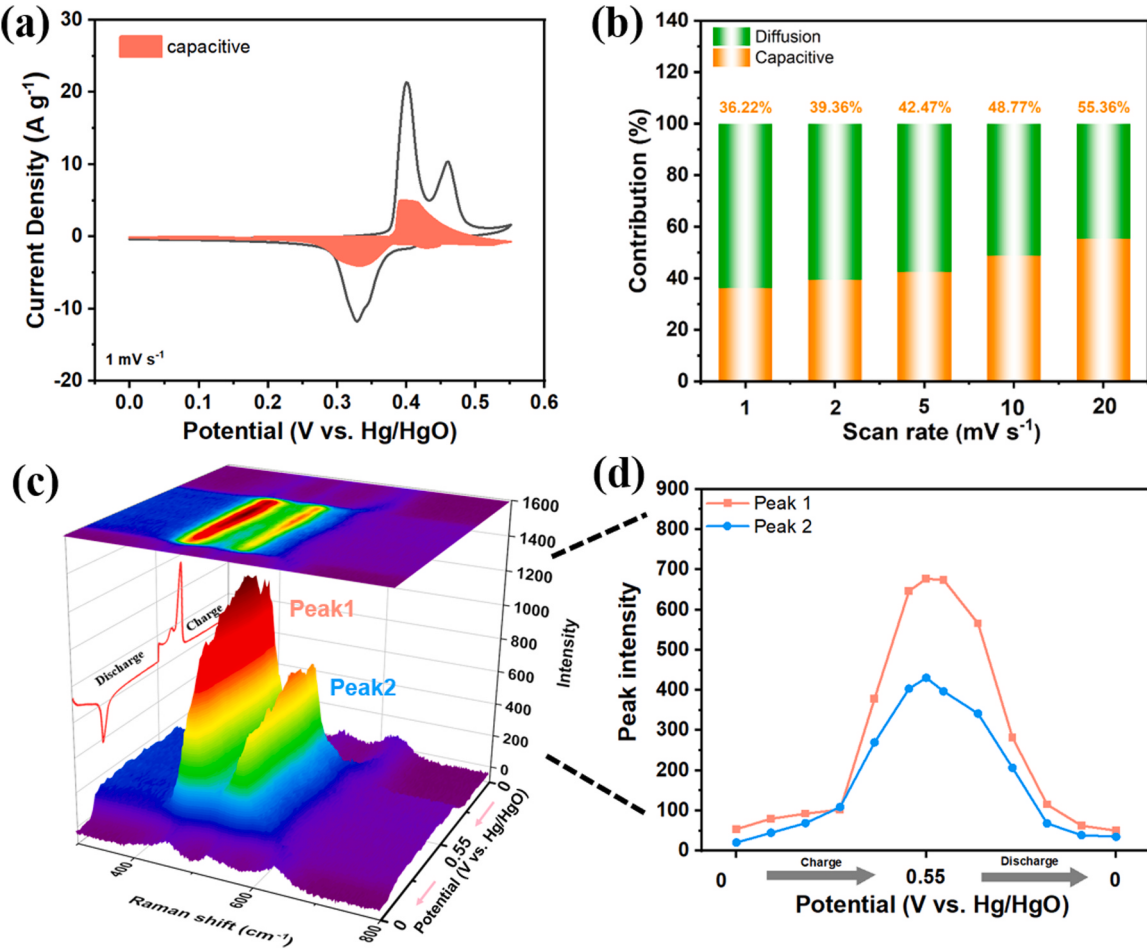


Fig. 6. (a) CV curve with the shaded area showing surface capacitive contribution at 1 mV s^{-1} . (b) Surface capacitive and diffusion-controlled contribution at the scan rates from 1 to 20 mV s^{-1} . (c) In-situ Raman spectra of Vo-NiMnMg-LDH@3DG during the charging/discharging process (1 mV s^{-1}). (d) The change for the typical peak area and intensity in (c).

peaks during the charge-discharge cycle. Overall, the in-situ Raman result validates that the reversible redox reaction of $\text{Ni}^{2+}/\text{Ni}^{3+}$ and $\text{Mn}^{2+}/\text{Mn}^{3+}$ takes place and contributes to the charge storage of our Vo-NiMnMg-LDH/3DG.

To further assess the possibility of Vo-NiMnMg-LDH in practical energy-storage application, an asymmetric supercapacitor (ASC) was fabricated using Vo-NiMnMg-LDH@3DG as the cathode material and commercial AC as the anode material in 2 M KOH aqueous electrolyte, as illustrated in Fig. 7a. The optimal mass ratio of the cathode to anode is 1:2. Electrochemical performance of the AC electrode is presented in Figure S16, characterized by typical double-layer capacitance with rectangular CV curves and symmetric GCD profiles. Fig. 7b displays the CV curves of the Vo-NiMnMg-LDH@3DG and AC electrodes at 2 mV s^{-1} in a three-electrode system. Based on the complementary potential windows of the cathode (0–0.55 V) and the anode (-1.0–0 V), a working voltage of 1.55 V is expected for the ASC. To ensure the stability of the device over an extended period, 1.5 V is selected as the operating voltage of the assembled ASC. Fig. 7c shows CV curves of the Vo-NiMnMg-LDH@3DG//AC at different scan rates from 5 to 100 mV s^{-1} . The quasi-rectangular CV shape suggests the pseudocapacitive nature. Particularly, the ASC device still maintains the similar CV shape without obvious distortion even at a high scan rate of 100 mV s^{-1} , demonstrating the good rate capability. From the GCD curves in Fig. 7d, it is evident that the ASC has symmetric charge-discharge profiles, suggesting the high coulombic efficiency. The specific capacitance of the device is calculated based on the discharge process, which is displayed in Fig. 7e. To be more specific, the specific capacitance is 171.7, 124,

101.3, 85, and 82.4 F g^{-1} at the current density of 1, 2, 4, 8, and 10 A g^{-1} , respectively. Remarkably, even as the current density increase from 1 to 10 A g^{-1} , the ASC still retains 47.9% of the initial specific capacitance, revealing its satisfactory rate capability. Fig. 7f shows the Ragone plot for the Vo-NiMnMg-LDH@3DG//AC device. Impressively, a maximum energy density of 53.62 Wh kg^{-1} can be achieved at a power density of 749.9 W kg^{-1} and a high energy density of 25.75 Wh kg^{-1} is still maintained even as the power density is increased to 7500 W kg^{-1} . This energy density outperforms many reported LDH-based ASC devices (Table S8), such as Ov-NiMn-LDH//AC (46.7 Wh kg^{-1} at 1.7 kW kg^{-1}), [49] NiMn-LDH-O//AC (48.9 Wh kg^{-1} at 0.81 kW kg^{-1}), [54] NiMn-LDH/PC//AC (18.60 Wh kg^{-1} at 225.03 W kg^{-1}), [55] Co₃O₄@-NiMn-LDH//AC (47.15 Wh kg^{-1} at 316 W kg^{-1}), [61] NiC_o-LDH@C//RGO (45.02 Wh kg^{-1} at 799.96 W kg^{-1}) [62] and IPC/NiCoMn-LDH//IPC (40 Wh kg^{-1} at 0.8 kW kg^{-1}) [15]. Strikingly, even after 20,000 charge/discharge cycles at a current density of 5 A g^{-1} , the ASC still demonstrates a capacitance retention of 82.7% and a coulombic efficiency of near 100% (Fig. 7g), highlighting the exceptional cycling stability. SEM observation reveals that the nanosheet structure of the NiMnMg-LDH is still well-preserved after the long-term cycling (Figure S17), showcasing the excellent structural robustness of Vo-NiMnMg-LDH/3DG. To further understand the excellent cycling stability, both Nyquist and Bode plots are measured for the ASC device before and after cycling. As shown in Figure S18, after 20,000 cycles, the R_{ct} increases obviously from 7.2 to 14.8Ω , while the R_s shows only a negligible increase (Table S9), accompanied by a small increase in the time constant (τ_i). This might be attributed to the diminished surface

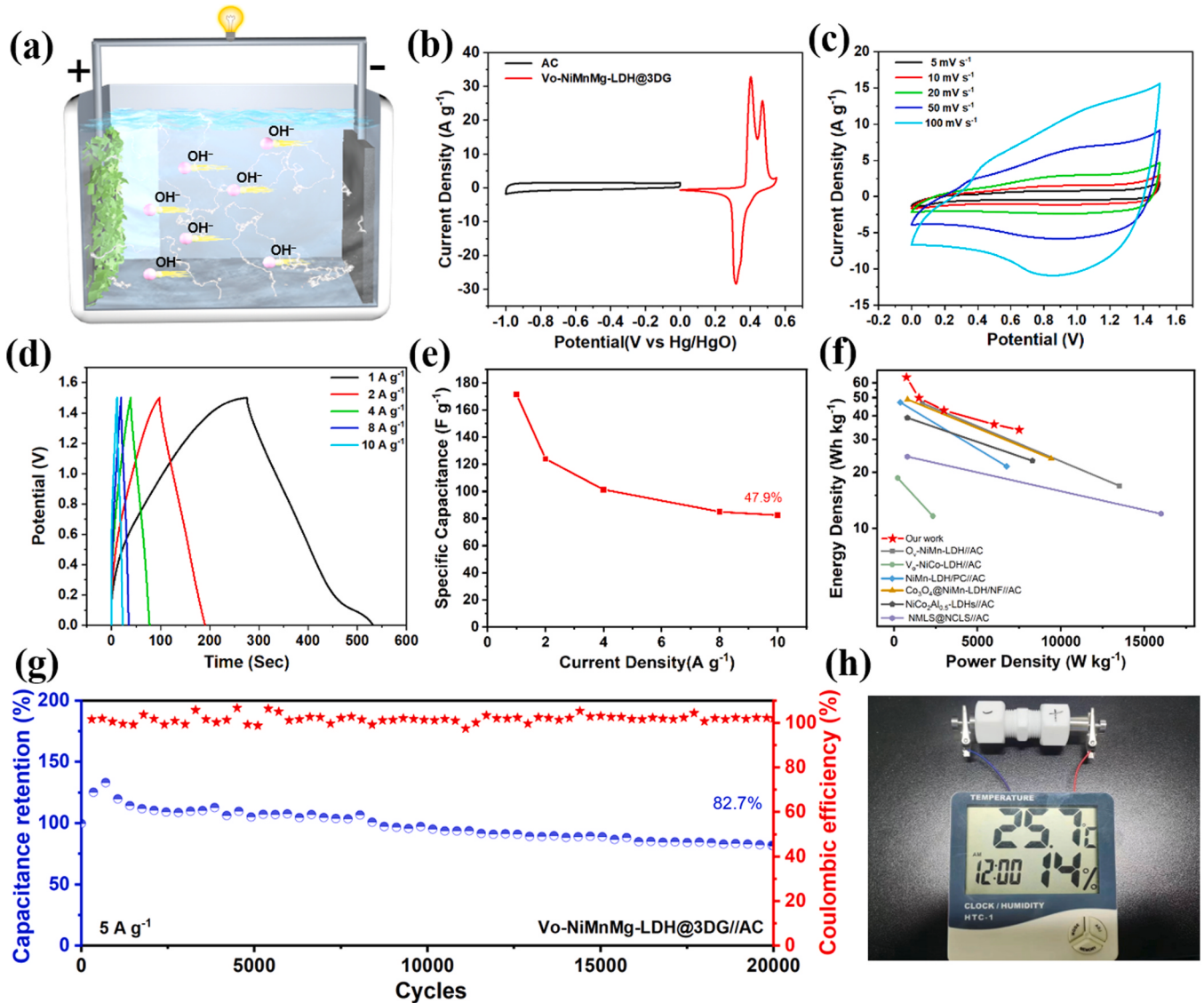


Fig. 7. (a) Schematic of as-fabricated ASC device. (b) CV curves of Vo-NiMnMg-LDH@3DG positive electrode and AC negative electrode at 2 mV s^{-1} . Electrochemical performance of the ASC device: (c) CV curves at different scan rates, (d) GCD curves at different current densities, (e) Specific capacitance at different current densities, (f) Ragone plots, (g) Cycling performance for 20,000 cycles at 5 A g^{-1} . (h) The photo of a thermal hygrometer powdered by the ASC device.

area and depletion of active sites during the prolonged cycling process. [63] The thermal hygrometer powered by the Vo-NiMnMg-LDH//AC device can operate successfully (Fig. 7h). More encouragingly, two ASCs in series can drive a fan to rotate at high speed for 50 s (Movie S1), which further illustrates the promising future of our electrode materials in energy storage applications.

Supplementary material related to this article can be found online at doi:10.1016/j.nanoen.2024.109690.

3. Conclusions

In summary, oxygen vacancy engineered NiMnMg-LDH anchored on 3D graphene foam is successfully fabricated through a two-step approach involving Mg doping during hydrothermal growth and subsequent Ar plasma etching. Doping of the non-electroactive Mg element not only stabilizes the NiMn-LDH lattice but also favors the formation of oxygen vacancies. Subsequent plasma treatment further increases the concentration of oxygen vacancies. Benefiting from the doping effect and oxygen vacancy engineering, the binder-free Vo-NiMnMg-LDH@3DG electrode delivers a high specific capacity of 374.8 mAh g^{-1}

at 1 A g^{-1} and excellent rate capability with a specific capacity of 278.3 mAh g^{-1} at 20 A g^{-1} . Moreover, the assembled ASC device with o-NiMnMg-LDH@3DG cathode and AC anode displays a specific capacitance up to 171 F g^{-1} at 1 A g^{-1} and the maximum energy density of 53.62 Wh kg^{-1} at a power density of 749.9 W kg^{-1} . Even after 20000 charge/discharge cycles at 5 A g^{-1} , the ASC still exhibits the remarkable stability with a capacitance retention of 82.7%. This work provides a facile but efficient way to enhance capacitive performance of LDH electrode by oxygen vacancy engineering.

CRediT authorship contribution statement

Bin Zhao: Writing – review & editing, Supervision, Funding acquisition. **Zhuo Wang:** Validation, Conceptualization. **Ming Xu:** Writing – review & editing, Resources. **Kun Fang:** Data curation. **Jiawei Wang:** Methodology. **Jingyuan Zhang:** Investigation. **Huajian Li:** Visualization. **Tianpeng Li:** Writing – original draft, Investigation, Data curation. **Yuting Hu:** Formal analysis, Data curation.

Declaration of Competing Interest

The authors declare that they have no known competing financial interests or personal relationships that could have appeared to influence the work reported in this paper.

Data availability

Data will be made available on request.

Acknowledgements

The authors gratefully acknowledge financial support from the National Natural Science Foundation of China (22209114, 52302287), the Natural Science Foundation of Shanghai (21ZR1445700), Shanghai Sailing Program (21YF1430800), and the Science and Technology Commission of Shanghai Municipality (23440790402).

Appendix A. Supporting information

Supplementary data associated with this article can be found in the online version at [doi:10.1016/j.nanoen.2024.109690](https://doi.org/10.1016/j.nanoen.2024.109690).

References

- [1] R. Kumar, S. Sahoo, E. Joanni, R.K. Singh, A review on the current research on microwave processing techniques applied to graphene-based supercapacitor electrodes: an emerging approach beyond conventional heating, *J. Energy Chem.* 74 (2022) 252–282, <https://doi.org/10.1016/j.jecchem.2022.06.051>.
- [2] W. Xu, X. Zhao, F. Zhan, Q. He, H. Wang, J. Chen, H. Wang, X. Ren, L. Chen, Toward emerging two-dimensional nickel-based materials for electrochemical energy storage: progress and perspectives, *Energy Storage Mater.* 53 (2022) 79–135, <https://doi.org/10.1016/j.ensm.2022.08.039>.
- [3] B. Ramulu, S. Chandra Sekhar, S.J. Arbaz, J.S. Yu, Nano-Ag laminated ternary layered double hydroxides for hybrid supercapacitors, *Chem. Eng. J.* 420 (2021) 130376, <https://doi.org/10.1016/j.cej.2021.130376>.
- [4] X. Li, D. Du, Y. Zhang, W. Xing, Q. Xue, Z. Yan, Layered double hydroxides toward high-performance supercapacitors, *J. Mater. Chem. A* 5 (30) (2017) 15460–15485, <https://doi.org/10.1039/c7ta04001f>.
- [5] J. Zhao, C. Ge, Z. Zhao, Q. Wu, M. Liu, M. Yan, L. Yang, X. Wang, Z. Hu, Sub-nanometer-scale fine regulation of interlayer distance in Ni-Co layered double hydroxides leading to high-rate supercapacitors, *Nano Energy* 76 (2020) 105026, <https://doi.org/10.1016/j.nanoen.2020.105026>.
- [6] W. Guo, C. Yu, C. Zhao, Z. Wang, S. Li, J. Yu, X. Tan, Y. Xie, L. Yang, H. Huang, R. Fu, J. Qiu, Boosting charge storage in 1D manganese oxide-carbon composite by phosphorus-assisted structural modification for supercapacitor applications, *Energy Storage Mater.* 31 (2020) 172–180, <https://doi.org/10.1016/j.ensm.2020.06.008>.
- [7] H. Wang, X. Ren, J. Chen, W. Xu, Q. He, H. Wang, F. Zhan, L. Chen, Recent advances of emerging oxyhydroxide for electrochemical energy storage applications, *J. Power Sources* 554 (2023) 232309, <https://doi.org/10.1016/j.jpowsour.2022.232309>.
- [8] J. Ma, J. Xia, Z. Liang, X. Chen, Y. Du, C.H. Yan, Layered double hydroxide hollowcages with adjustable layer spacing for high performance hybrid supercapacitor, *Small* 17 (49) (2021) 2104423, <https://doi.org/10.1002/smll.202104423>.
- [9] Q. Yang, Z. Li, B. Xu, Layered double hydroxide with interlayer quantum dots and laminate defects for high-performance supercapacitor, *Adv. Funct. Mater.* 33 (24) (2023) 2300149, <https://doi.org/10.1002/adfm.202300149>.
- [10] H. Zhang, Y. Lv, X. Wu, J. Guo, D. Jia, Electrodeposition synthesis of high performance MoO₃-x@Ni-Co layered double hydroxide hierarchical nanorod arrays for flexible solid-state supercapacitors, *Chem. Eng. J.* 431 (2022) 133233, <https://doi.org/10.1016/j.cej.2021.133233>.
- [11] M. Tian, C. Liu, Z.G. Neale, J. Zheng, D. Long, G. Cao, Chemically Bonding NiFe-LDH nanosheets on rGO for superior lithium-ion capacitors, *ACS Appl. Mater. Interfaces* 11 (39) (2019) 35977–35986, <https://doi.org/10.1021/acsmami.9b10719>.
- [12] X. Wang, H. Li, H. Li, S. Lin, J. Bai, J. Dai, C. Liang, X. Zhu, Y. Sun, S. Dou, Heterostructures of Ni-Co-Al layered double hydroxide assembled on V₄C₃MXene for high-energy hybrid supercapacitors, *J. Mater. Chem. A* 7 (5) (2019) 2291–2300, <https://doi.org/10.1039/c8ta11249e>.
- [13] Q. Li, C. Lu, C. Chen, L. Xie, Y. Liu, Y. Li, Q. Kong, H. Wang, Layered NiCo₂O₄/reduced graphene oxide composite as an advanced electrode for supercapacitor, *Energy Storage Mater.* 8 (2017) 59–67, <https://doi.org/10.1016/j.ensm.2017.04.002>.
- [14] L. Xu, Y. Li, M. Li, N. Yu, W. Wang, F. Wei, J. Qi, Y. Sui, L. Li, L. Zhang, Mo-doped NiCo-LDH nanoflower derived from ZIF-67 nanosheet arrays for high-performance supercapacitors, *J. Energy Storage* 77 (2024) 109781, <https://doi.org/10.1016/j.est.2023.109781>.
- [15] Z. Lu, K. Zhao, H. Guo, L. Duan, H. Sun, K. Chen, J. Liu, In Situ Construction of NiCoMn-LDH derived from zeolitic imidazolate framework on eggshell-like carbon skeleton for high-performance flexible supercapacitors, *Small* (2023) 2309814, <https://doi.org/10.1002/smll.202309814>.
- [16] C. Jiang, B. Zhao, J. Cheng, J. Li, H. Zhang, Z. Tang, J. Yang, Hydrothermal synthesis of Ni(OH)₂ nanoflakes on 3D graphene foam for high-performance supercapacitors, *Electrochim. Acta* 173 (2015) 399–407, <https://doi.org/10.1016/j.electacta.2015.05.081>.
- [17] W. Hu, L. Chen, X. Wu, M. Du, Y. Song, Z. Wu, Q. Zheng, Slight zinc doping by an ultrafast electrodeposition process boosts the cycling performance of layered double hydroxides for ultralong-life-span supercapacitors, *ACS Appl. Mater. Interfaces* 13 (32) (2021) 38346–38357, <https://doi.org/10.1021/acsmami.1c10386>.
- [18] Y. Ding, Z. Yan, G. Wang, H. Sang, Z. Xu, W. Li, Regulating the oxygen vacancy and electronic structure of NiCo layered double hydroxides by molybdenum doping for high-power hybrid supercapacitors, *Small* 20 (2024) 2306382, <https://doi.org/10.1002/smll.202306382>.
- [19] X. Gao, X. Liu, D. Wu, B. Qian, Z. Kou, Z. Pan, Y. Pang, L. Miao, J. Wang, Significant role of Al in ternary layered double hydroxides for enhancing electrochemical performance of flexible asymmetric supercapacitor, *Adv. Funct. Mater.* 29 (36) (2019) 1903879, <https://doi.org/10.1002/adfm.201903879>.
- [20] X. Hong, E. Zhu, Z. Ye, K.S. Hui, K.N. Hui, Enhanced phosphate removal under an electric field via multiple mechanisms on MgAl-LDHs/AC composite electrode, *J. Electroanal. Chem.* 836 (2019) 16–23, <https://doi.org/10.1016/j.jelechem.2019.01.046>.
- [21] S. Jiang, Y. Qiao, T. Fu, W. Peng, T. Yu, B. Yang, R. Xia, M. Gao, Integrated battery-capacitor electrodes: pyridinic N-doped porous carbon-coated abundant oxygen vacancy Mn-Ni-layered double oxide for hybrid supercapacitors, *ACS Appl. Mater. Interfaces* 13 (29) (2021) 34374–34384, <https://doi.org/10.1021/acsmami.1c08699>.
- [22] W. Guo, C. Yu, S. Li, X. Song, H. Huang, X. Han, Z. Wang, Z. Liu, J. Yu, X. Tan, J. Qiu, A universal converse voltage process for triggering transition metal hybrids in situ phase restriction toward ultrahigh-rate supercapacitors, *Adv. Mater.* 31 (28) (2019) 1901241, <https://doi.org/10.1002/adma.201901241>.
- [23] S. Li, N. Sharma, C. Yu, Y. Zhang, G. Wan, R. Fu, H. Huang, X. Sun, S.-J. Lee, J.-S. Lee, D. Nordlund, P. Pianetta, K. Zhao, Y. Liu, J. Qiu, Operando tailoring of defects and strains in corrugated β-Ni(OH)₂ nanosheets for stable and high-rate energy storage, *Adv. Mater.* 33 (2) (2021) 2006147, <https://doi.org/10.1002/adma.202006147>.
- [24] H. Liang, H. Jia, T. Lin, Z. Wang, C. Li, S. Chen, J. Qi, J. Cao, W. Fei, J. Feng, Oxygen-vacancy-rich nickel-cobalt layered double hydroxide electrode for high-performance supercapacitors, *J. Colloid Interf. Sci.* 554 (2019) 59–65, <https://doi.org/10.1016/j.jcis.2019.06.095>.
- [25] G. Wang, Z. Jin, Oxygen-vacancy-rich cobalt-aluminium hydrotalcite structures served as high-performance supercapacitor cathode, *J. Mater. Chem. C* 9 (2) (2021) 620–632, <https://doi.org/10.1039/d0tc03640d>.
- [26] H. Zhang, Y. Bai, H. Chen, J. Wu, C.M. Li, X. Su, L. Zhang, Oxygen-defect-rich 3D porous cobalt-gallium layered double hydroxide for high-performance supercapacitor application, *J. Colloid Interf. Sci.* 608 (2022) 1837–1845, <https://doi.org/10.1016/j.jcis.2021.10.109>.
- [27] S. Li, Y. Zhang, N. Liu, C. Yu, S.-J. Lee, S. Zhou, R. Fu, J. Yang, W. Guo, H. Huang, J.-S. Lee, C. Wang, T.R. Kim, D. Nordlund, P. Pianetta, X. Du, J. Zhao, Y. Liu, J. Qiu, Operando revealing dynamic reconstruction of NiCo carbonate hydroxide for high-rate energy storage, *Joule* 4 (3) (2020) 673–687, <https://doi.org/10.1016/j.joule.2020.01.018>.
- [28] C. Jing, B. Dong, Y. Zhang, Chemical modifications of layered double hydroxides in the supercapacitor, *Energy Environ. Mater.* 3 (3) (2020) 346–379, <https://doi.org/10.1002/eem.212116>.
- [29] W. Guo, F. Yang, C. Yu, Y. Xie, J. Chen, Y. Liu, Y. Zhao, J. Yang, X. Feng, S. Li, Z. Wang, J. Yu, K. Liu, B. Qian, M. Tsige, Q. Zhang, J. Guo, J. Qiu, Operando leaching of pre-incorporated Al and mechanism in transition-metal hybrids on carbon substrates for enhanced charge storage, *Matter* 4 (9) (2021) 2902–2918, <https://doi.org/10.1016/j.matt.2021.06.035>.
- [30] S. Dou, L. Tao, R. Wang, S. El Hankari, R. Chen, S. Wang, Plasma-assisted synthesis and surface modification of electrode materials for renewable energy, *Adv. Mater.* 30 (21) (2018) 1705850, <https://doi.org/10.1002/adma.201705850>.
- [31] C. Lin, J. Li, Z.W. Yin, W. Huang, Q. Zhao, Q. Weng, Q. Liu, J. Sun, G. Chen, F. Pan, Structural understanding for high-voltage stabilization of lithium cobalt oxide, *Adv. Mater.* (2023) 2307404, <https://doi.org/10.1002/adma.202307404>.
- [32] Y. Cheng, X. Wang, D. Zhang, X. Qiao, H. Zhao, L. Chang, Z. Yu, Y. Xia, J. Fan, C. Huang, S. Yang, High-capacity binderless supercapacitor electrode obtained from sulfidation large interlayer spacing of NiMn-LDH, *Electrochim. Acta* 429 (2022) 141039, <https://doi.org/10.1016/j.electacta.2022.141039>.
- [33] V. Sharma, M. Aman, S. Omar, NiMn-layered double hydroxide porous nanoarchitectures as a bifunctional material for accelerated p-nitrophenol reduction and freestanding supercapacitor electrodes, *ACS Appl. Nano Mater.* 5 (10) (2022) 15651–15664, <https://doi.org/10.1021/acsanm.2c03719>.
- [34] X. Yue, Y. Dong, H. Cao, X. Wei, Q. Zheng, W. Sun, D. Lin, Effect of electronic structure modulation and layer spacing change of NiAl layered double hydroxide nanoflowers caused by cobalt doping on supercapacitor performance, *J. Colloid Interf. Sci.* 630A (2023) 973–983, <https://doi.org/10.1016/j.jcis.2022.10.033>.
- [35] Y. Tang, Q. Liu, L. Dong, H.B. Wu, X.-Y. Yu, Activating the hydrogen evolution and overall water splitting performance of NiFe LDH by cation doping and plasma

- reduction, *Appl. Catal. B-Environ.* 266 (2020) 118627, <https://doi.org/10.1016/j.apcatb.2020.118627>.
- [36] E.J. Heller, Y. Yang, L. Kocia, W. Chen, S. Fang, M. Borunda, E. Kaxiras, Theory of graphene Raman scattering, *ACS Nano* 10 (2) (2016) 2803–2818, <https://doi.org/10.1021/acsnano.5b07676>.
- [37] H. Ren, L. Zhang, J. Zhang, T. Miao, R. Yuan, W. Chen, Z. Wang, J. Yang, B. Zhao, Na⁺ pre-intercalated Na_{0.11}MnO₂ on three-dimensional graphene as cathode for aqueous zinc ion hybrid supercapacitor with high energy density, *Carbon* 198 (2022) 46–56, <https://doi.org/10.1016/j.carbon.2022.07.008>.
- [38] W. Guo, C. Dun, C. Yu, X. Song, F. Yang, W. Kuang, Y. Xie, S. Li, Z. Wang, J. Yu, G. Fu, J. Guo, M.A. Marcus, J.J. Urban, Q. Zhang, J. Qiu, Mismatching integration-enabled strains and defects engineering in LDH microstructure for high-rate and long-life charge storage, *Nat. Commun.* 13 (1) (2022) 1409, <https://doi.org/10.1038/s41467-022-28918-0>.
- [39] M. Gao, Y. Li, J. Yang, Y. Liu, Y. Liu, X. Zhang, S. Wu, K. Cai, Nickel-cobalt (oxy) hydroxide battery-type supercapacitor electrode with high mass loading, *Chem. Eng. J.* 429 (2022) 132423, <https://doi.org/10.1016/j.cej.2021.132423>.
- [40] S.A. Chala, M.-C. Tsai, W.-N. Su, K.B. Ibrahim, B. Thirumalraj, T.-S. Chan, J.-F. Lee, H. Dai, B.-J. Hwang, Hierarchical 3D Architected Ag nanowires shelled with NiMn-layered double hydroxide as an efficient bifunctional oxygen electrocatalyst, *ACS Nano* 14 (2) (2020) 1770–1782, <https://doi.org/10.1021/acsnano.9b07487>.
- [41] X. Yang, H. Zhang, W. Xu, B. Yu, Y. Liu, Z. Wu, A doping element improving the properties of catalysis: in situ Raman spectroscopy insights into Mn-doped NiMn layered double hydroxide for the urea oxidation reaction, *Catal. Sci. Technol.* 12 (14) (2022) 4471–4485, <https://doi.org/10.1039/D2CY00308B>.
- [42] W. Wang, N. Zhang, Z. Shi, Z. Ye, Q. Gao, M. Zhi, Z. Hong, Preparation of Ni-Al layered double hydroxide hollow microspheres for supercapacitor electrode, *Chem. Eng. J.* 338 (2018) 55–61, <https://doi.org/10.1016/j.cej.2018.01.024>.
- [43] A.B. Trench, T.R. Machado, A.F. Gouveia, M. Assis, L.G. da Trindade, C. Santos, A. Perrin, C. Perrin, M. Oliva, J. Andrés, E. Longo, Connecting structural, optical, and electronic properties and photocatalytic activity of Ag₃Po₄:Mo complemented by DFT calculations, *Appl. Catal. B-Environ.* 238 (2018) 198–211, <https://doi.org/10.1016/j.apcatb.2018.07.019>.
- [44] Z. Jiao, Y. Chen, M. Du, M. Demir, F. Yan, W. Xia, Y. Zhang, C. Wang, M. Gu, X. Zhang, J. Zou, 3D hollow NiCo LDH nanocages anchored on 3D CoO sea urchin-like microspheres: a novel 3D/3D structure for hybrid supercapacitor electrodes, *J. Colloid Interf. Sci.* 633 (2023) 723–736, <https://doi.org/10.1016/j.jcis.2022.11.131>.
- [45] L. Chen, Y. Zhang, D. Li, Y. Wang, C. Duan, Magnesium-regulated oxygen vacancies of nickel layered double hydroxides for electrocatalytic water oxidation, *J. Mater. Chem. A* 6 (38) (2018) 18378–18383, <https://doi.org/10.1039/c8ta04615h>.
- [46] J. He, X. Zhou, P. Xu, J. Sun, Promoting electrocatalytic water oxidation through tungsten-modulated oxygen vacancies on hierarchical FeNi-layered double hydroxide, *Nano Energy* 80 (2021) 105540, <https://doi.org/10.1016/j.nanoen.2020.105540>.
- [47] W. He, J. Li, Y. Zhang, J. Yang, T. Zeng, N. Yang, High-Performance supercapacitors using hierarchical and sulfur-doped trimetallic NiCo/NiMn layered double hydroxides, *Small Methods* (2023) 2301167, <https://doi.org/10.1002/smtd.202301167>.
- [48] J. Hong, C. Chen, A. Siriviriyaranun, D.G. Crivoi, P. Holdway, J.C. Buffet, D. O'Hare, Ni(2)Mn-layered double oxide electrodes in organic electrolyte based supercapacitors, *RSC Adv.* 11 (44) (2021) 27267–27275, <https://doi.org/10.1039/dra04681k>.
- [49] Y. Tang, H. Shen, J. Cheng, Z. Liang, C. Qu, H. Tabassum, R. Zou, Fabrication of oxygen-vacancy abundant NiMn-layered double hydroxides for ultrahigh capacity supercapacitors, *Adv. Funct. Mater.* 30 (11) (2020) 1908223, <https://doi.org/10.1002/adfm.201908223>.
- [50] G. Zhou, X. Gao, S. Wen, X. Wu, L. Zhang, T. Wang, P. Zhao, J. Yin, W. Zhu, Magnesium-regulated oxygen vacancies of cobalt-nickel layered double hydroxide nanosheets for ultrahigh performance asymmetric supercapacitors, *J. Colloid Interf. Sci.* 612 (2022) 772–781, <https://doi.org/10.1016/j.jcis.2021.12.087>.
- [51] Q. Huang, Y. Chen, H. Yu, L. Yan, J. Zhang, B. Wang, B. Du, L. Xing, Magnetic graphene oxide/MgAl-layered double hydroxide nanocomposite: one-pot solvothermal synthesis, adsorption performance and mechanisms for Pb²⁺, Cd²⁺, and Cu²⁺, *Chem. Eng. J.* 341 (2018) 1–9, <https://doi.org/10.1016/j.cej.2018.01.156>.
- [52] S. Liu, J. Zhu, M. Sun, Z. Ma, K. Hu, T. Nakajima, X. Liu, P. Schmuki, L. Wang, Promoting the hydrogen evolution reaction through oxygen vacancies and phase transformation engineering on layered double hydroxide nanosheets, *J. Mater. Chem. A* 8 (5) (2020) 2490–2497, <https://doi.org/10.1039/c9ta12768b>.
- [53] K. Chen, Y.-H. Cao, S. Yadav, G.C. Kim, Z. Han, W. Wang, W.-J. Zhang, V. Dao, I.-H. Lee, Electronic structure reconfiguration of nickel–cobalt layered double hydroxide nanoflakes via engineered heteroatom and oxygen-vacancies defect for efficient electrochemical water splitting, *Chem. Eng. J.* 463 (2023) 142396, <https://doi.org/10.1016/j.cej.2023.142396>.
- [54] Y. Tang, Z. Liang, Y. Jin, S. Gao, R. Zou, Understanding and tackling lattice manganese exfoliation and deactivation of battery-type NiMn-LDH in fast electrochemical energy storage, *J. Mater. Chem. A* 9 (40) (2021) 23286–23295, <https://doi.org/10.1039/d1ta06481a>.
- [55] M. Yu, R. Liu, J. Liu, S. Li, Y. Ma, Polyhedral-Like NiMn-Layered Double Hydroxide/Porous Carbon as Electrode for Enhanced Electrochemical Performance Supercapacitors, *Small* 13 (44) (2017) 1702616, <https://doi.org/10.1002/smll.201702616>.
- [56] D. Zhang, J. Cao, X. Zhang, N. Insin, R. Liu, J. Qin, NiMn layered double hydroxide nanosheets in-situ anchored on Ti₃C₂ MXene via chemical bonds for superior supercapacitors, *ACS Appl. Energy Mater.* 3 (6) (2020) 5949–5964, <https://doi.org/10.1021/acsaem.0c00863>.
- [57] L. Yao, Q. Wu, P. Zhang, J. Zhang, D. Wang, Y. Li, X. Ren, H. Mi, L. Deng, Z. Zheng, Scalable 2D hierarchical porous carbon nanosheets for flexible supercapacitors with ultrahigh energy density, *Adv. Mater.* 30 (11) (2018) 1706054, <https://doi.org/10.1002/adma.201706054>.
- [58] R. Zhang, J. Dong, W. Zhang, L. Ma, Z. Jiang, J. Wang, Y. Huang, Synergistically coupling of 3D FeNi-LDH arrays with Ti₃C₂T_x-MXene nanosheets toward superior symmetric supercapacitor, *Nano Energy* 91 (2022) 106633, <https://doi.org/10.1016/j.nanoen.2021.106633>.
- [59] H. Wang, W. Jiang, S. Chen, J. Chen, F. Wu, R. Liang, Epitaxial oriented growth of LDH on Few-Layer graphene/microporous carbon heterostructure sheets for asymmetric supercapacitor application, *Chem. Eng. J.* 474 (2023) 145755, <https://doi.org/10.1016/j.cej.2023.145755>.
- [60] T.T. Yin, H.M. Xu, X.L. Zhang, X. Su, L. Shi, C. Gu, S.K. Han, Mn-Incorporation-induced phase transition in bottom-up synthesized colloidal Sub-1nm Ni(OH)₂ nanosheets for enhanced oxygen evolution catalysis, *Nano Lett.* 23 (8) (2023) 3259–3266, <https://doi.org/10.1021/acs.nanolett.3c00067>.
- [61] W. Huang, A. Zhang, X. Li, J. Tian, L. Yue, L. Cui, R. Zheng, D. Wei, J. Liu, Multilayer NiMn layered double hydroxide nanosheets covered porous Co₃O₄ nanowire arrays with hierarchical structure for high-performance supercapacitors, *J. Power Sources* 440 (2019) 227123, <https://doi.org/10.1016/j.jpowsour.2019.227123>.
- [62] J. Yuan, Y. Li, G. Lu, Z. Gao, F. Wei, J. Qi, Y. Sui, Q. Yan, S. Wang, Controlled synthesis of flower-like hierarchical NiCo-layered double hydroxide integrated with metal-organic framework-derived Co@C for supercapacitors, *ACS Appl. Mater. Interfaces* 15 (30) (2023) 36143–36153, <https://doi.org/10.1021/acsmami.3c00561>.
- [63] M. Sajjad, R. Tao, K. Kang, S. Luo, L. Qiu, Phosphine-based porous organic polymer/rGO aerogel composites for high-performance asymmetric supercapacitor, *ACS Appl. Energy Mater.* 4 (2021) 828–838, <https://doi.org/10.1021/acsae.0c02725>.



Tianpeng Li received his bachelor's degree from Chengdu University of Technology in 2020, and he is currently a master student under the supervision of Prof. Bin Zhao at School of Materials and Chemistry, University of Shanghai for Science and Technology. His current research focuses on the preparation, structure optimization and electrochemical



Yuting Hu received her bachelor's degrees from Shanghai Institute of Technology in Materials Science and Engineering. Now she is a master student supervised by Prof. Bin Zhao at School of Materials and Chemistry, University of Shanghai for Science and Technology. Her current research interests are electrochemical energy storage materials and devices.



Jingyuan Zhang received her master degree from Bohai University in 2021. She is currently a doctoral student supervised by Prof. Bin Zhao at School of Materials and Chemistry, University of Shanghai for Science and Technology. The current research focus is MOF-based electrocatalytic materials for water splitting and biomass oxidation.



Huajian Li received his bachelor's degree from Northeastern University in 2020. He is currently pursuing a Ph.D. degree in the group of Prof. Ming Xu at Huazhong University of Science and Technology. His research interest is nanocarbon-based underwater pressure sensor.



Jiawei Wang received his master degree from University of Science and Technology Beijing in 2018, and then he obtained his PhD degree in School of Chemistry at Beihang University in 2023. Now he is a lecturer in School of Materials and Chemistry at University of Shanghai for Science and Technology. His research focuses on zinc ion batteries.



Kun Fang received his bachelor's degree from Anhui University of Science and Technology in 2022. He is currently a master student under the supervision of Prof. Bin Zhao at School of Materials and Chemistry, University of Shanghai for Science and Technology. My current research focuses on the positive electrode materials of water zinc-ion hybrid supercapacitors



Ming Xu obtained her bachelor's degree in 2003 and Ph.D. degree in 2007 from Shanghai Jiao Tong University. She conducted research in renowned institutions in Japan and the USA. Since 2012, she has been a full professor at Huazhong University of Science and Technology. Her research interest is development of nanocarbon-based multifunctional materials.



Zhuo Wang received her Ph.D. degree from Fudan University in 2020. She is currently working at School of Materials and Chemistry, University of Shanghai for Science and Technology. Her research interest mainly focuses on rechargeable zinc-ion batteries.



Bin Zhao obtained his Ph.D. degree in 2004 from Tsinghua University. Then, he conducted postdoctoral research in the University of Tokyo and National Institute of Advanced Industrial Science and Technology, Japan. Since 2009, he has joined University of Shanghai for Science and Technology as a full professor. His research interest is development of low-dimensional composites for energy storage and conversion.